Journal of Hazardous Materials 495 (2025) 138873

Contents lists available at ScienceDirect

Journal of Hazardous Materials

journal homepage: www.elsevier.com/locate/jhazmat

POM-promoted synergistic catalysis of NO and chlorobenzene over amorphous MnCeOx catalysts: Activation of lattice oxygen, role of acid site, catalytic mechanism

Shengyong Lu [a], Xuanhao Guo [a], Xinlei Xu [a], Zhengdong Han [a], Min Chen [a], Beilong Lin [a], Yaqi Peng [b], Guanjie Wang [a,*,1]

[a] Zhejiang Key Laboratory of Advanced Solid State Energy Storage Technology and Applications, Taizhou Institute of Zhejiang University, Taizhou 318000, China
[b] State Key Laboratory of Clean Energy Utilization, Institute for Thermal Power Engineering, Zhejiang University, Hangzhou 310027, China

HIGHLIGHTS

- The POM-structure increases the content of lattice oxygen, oxygen vacancies, and acid sites.
- The POM-SiW structure weakens the Mn-O bond and activates lattice oxygen through orbital polarization.
- The POM-SiW structure inhibits surface competitive adsorption and promotes the formation of NO2 and NH_4^+.

GRAPHICAL ABSTRACT

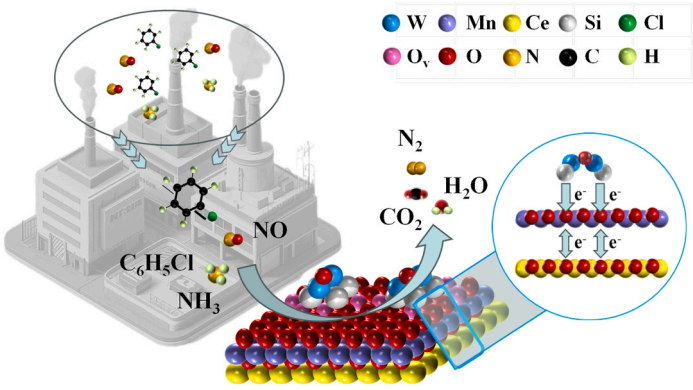

ARTICLE INFO

Keywords:
Polyoxometalates
NO_x
Mn-Ce bimetallic oxide
Lattice oxygen
Synergistic catalytic

ABSTRACT

The release rate of lattice oxygen and surface acidic sites are key factors for the multi-pollutant synergistic catalysis such as nitrogen oxides (NOx) and chlorine-containing volatile organic compounds (Cl-VOCs). In this study, a polyoxometalate (POM)-assisted strategy was employed to optimize the synergistic catalytic performance of MnCeOx for NO and chlorobenzene. The strong proton conductivity of the surface POM structure effectively suppresses the deposition of chlorinated species, preventing the poisoning of active sites. Specifically, POM-SiW structure can act as a dechlorination site in place of Mn_3O_4 and exhibits the highest density of acidic sites and oxygen vacancies, leading to a reduction of the T_{90} for chlorobenzene to 167 ℃ and an expansion. The assistance of POM-SiW structure facilitates the electron transfer from POM-SiW to lattice oxygen (O_{lat}), resulting in reduced orbital overlap between Mn and O atoms, thereby weakening the Mn-O bond and activating O_{lat}. Furthermore, in-situ DRIFTs, TOF-SIMS and DFT results confirmed that POM-SiW structure can inhibit the competitive adsorption of NO, NH_3 and chlorobenzene, NO_2 and NH_4^+ act as additional oxidants and

* Corresponding author.
E-mail address: gj-wang@zju.edu.cn (G. Wang).
[1] Mailing address: Taizhou Institute of Zhejiang University, Zhejiang University, Taizhou, 318000, China.

https://doi.org/10.1016/j.jhazmat.2025.138873
Received 3 March 2025; Received in revised form 30 May 2025; Accepted 8 June 2025
Available online 8 June 2025

dechlorinating agents, effectively promoting the catalytic decomposition of chlorobenzene and its intermediate products. This work provides a novel strategy for catalyst design in low-temperature multi-pollutant synergistic catalysis.

1. Introduction

The increasing reliance on municipal solid waste incineration technology has significantly contributed to large-scale emissions of pollutants such as nitrogen oxides (NOx) and chlorine-containing volatile organic compounds (Cl-VOCs), which are associated with environmental challenges including acid rain and the greenhouse effect [1–3]. Ammonia selective catalytic reduction (NH_3-SCR) is the most widely used and mature de-NOx technology [4]. Within the NH_3-SCR process, NOx is selectively reduced to N_2, with NO_2 serving as a reactive intermediate. Due to its strong oxidative properties, NO_2 can also facilitate the catalytic oxidation of Cl-VOCs [5]. Manganese-based catalysts have garnered significant attention for de-NOx applications due to their high nitrogen selectivity and effective catalytic performance at low temperatures (<200 ℃) [6]. However, these catalysts exhibit a catalytic temperature window of 200 ℃ to 400℃ for Cl-VOCs oxidation, with a marked decline in N_2 selectivity above 300 ℃. Furthermore, their susceptibility to chlorine poisoning poses a substantial challenge to achieving efficient synergistic removal of NOx and Cl-VOCs [7]. As a result, lowering the catalytic temperature for Cl-VOCs oxidation, mitigating chlorine poisoning, and preserving high N_2 selectivity have emerged as critical priorities in advancing multi-pollutant collaborative catalysis research.

The catalytic performance for Cl-VOCs can be enhanced through element doping and surface property optimization. However, such improvements often hinder the NH_3-SCR reaction. The rate-determining steps for both NH_3-SCR and Cl-VOCs oxidation are closely linked to the lattice oxygen release rate and the presence of surface acidic sites [8–10]. Consequently, targeted optimization of lattice oxygen mobility, oxygen vacancy content, and surface acidity is crucial for promoting the simultaneous catalytic reactions of NH_3-SCR and Cl-VOCs [11,12]. Li et al. improved the performance of MnO_2-CeO_2 catalysts by utilizing orbital polarization effects to limit electron transfer on the catalyst surface [13]. This approach balanced acidic and active sites, reducing the energy barrier for Cl-ion dissociation and HCl formation, while inhibiting the deposition of chlorine-containing species and N_2O formation. Additionally, Li et al. demonstrated that grafting polyoxometalates (POMs) onto catalysts could form a chain-like structure on the surface, protecting the active sites while inducing Brønsted acidity [14,15]. This technique effectively suppressed the formation of poly-chlorinated byproducts. The POM structure, with its highly tunable functional cluster frameworks and strong proton conductivity, provided the catalyst surface with additional acidic sites and active centers [16–19]. Moreover, the construction of heterogeneous interfaces often activates lattice oxygen [20], yet the relationship between the POM grafting technique and lattice oxygen remains unclear.

In this work, it was demonstrated that the strong proton conductivity of POM accelerates the release of oxygen from the lattice, and effectively enhance the low-temperature synergistic catalytic performance of NO and chlorobenzene (CB). The POM grafting technique significantly increased both the number of acidic sites and oxygen vacancies. The interaction between the surface POM-SiW structure and MnCeOx facilitated electron transfer from POM-SiW structure to MnCeOx, reducing the orbital overlap between Mn and O atoms in the active sites, and activating lattice oxygen. Intermediate products such as NH_4^+ and NO_2 further facilitated the dechlorination and conversion of CB at low temperatures. This study provides new insights for expanding the low-temperature synergistic catalytic temperature window for NOx and Cl-VOCs and for the design of efficient low-temperature catalysts.

2. Experiment

2.1. Catalyst preparation

The $KMnO_4$ solution (50 mL, 0.02 mol/L) was added dropwise into a mixture solution (50 mL) containing $Mn(NO_3)_2{\cdot}4H_2O$ (0.02 mol/L) and $Ce(NO_3)_3{\cdot}6H_2O$ (0.02 mol/L) while stirring for 2 h. The resulting mixture was then washed until neutral, followed by drying at 80 ℃ for 24 h. The dried product was subsequently calcined at 300℃ (2 ℃/min) for 4 h and labeled as $MnCeO_x$.

The hydrogen peroxide solution (10 mL, 0.25 mol/L) were added dropwise to the mixture solution containing 2 g $MnCeO_x$ and 0.06 g silicotungstic acid under stirring for 2 h at ambient temperature. After that, it was washed and dried at 80 ℃ for 24 h. The black powder was followed by calcining for 2 h at 300 ℃ to get $MnCeO_x$-SiW. For comparison, the silicomolybdic acid and phosphotungstic acid were replace the silicotungstic acid to prepare the $MnCeO_x$-SiMo and $MnCeO_x$-PW, respectively.

2.2. Catalyst characterization

The specific surface area, pore size, microscopic morphology, crystal structure, oxygen vacancy were explored by BET, SEM, TEM, XRD, EPR technologies. The electronic structure was examined using X-ray absorption fine structure (XAFS). Mn K-edge XAFS analyses were performed with Si (111) crystal monochromators at the BL14W1 beamline of the Shanghai Synchrotron Radiation Facility (SSRF), and the analysis and fitting were conducted using Artemis and IFEFFIT software.

The redox properties and acid content were evaluated by O_2-temperature-programmed desorption (O_2-TPD), NH_3-temperature-programmed desorption (NH_3-TPD), and H_2-temperature-programmed reduction (H_2-TPR) with chemisorption apparatus (VDSorb-91i). The changes in acid sites at different temperature were indentified by the pyridine infrared (Py-IR, Bruker Tensor27). The metal valence states were analyzed by X-ray photoelectron spectroscopy (XPS, Shimadzu/ Kratos Axis Supra). The C1s peak (284.8 eV) was used to correct for the transfer of binding energy due to surface charge. Detail description of characterizations involving BET, EPR, O_2-TPD, NH_3-TPD, etc., are also listed in the supporting information.

The material composition on the sample surface was analyzed using time-of-flight secondary ion mass spectrometry (TOF-SIMS, ION-TOF GmbH Germany) and in-situ diffuse fourier transform infrared spectroscopy (In-situ DRIFTs, Thermo Scientific Nicolet iS50/ Harrick HVC-DRM). The In-situ DRIFTs spectra (800–3900 cm^{-1}) were recorded with a resolution of 4 cm^{-1}.

All DFT calculations were performed by using the Vienna Ab initio Simulation package (VASP) and the detail information is described in the supporting information.

2.3. Catalytic activity evaluation

The performance of sample was evaluated in a continuous flow fixed-bed reactor under atmospheric pressure. A 200 mg sample (40–60 mesh particle size) was placed inside a quartz reactor (inner diameter = 8 mm) and secured with quartz wool at both ends. The flow rates were accurately controlled using mass flow controllers (MFCs), maintaining a gas mixture containing 100 ppm CB, 500 ppm NO, 500 ppm NH_3, and 11 % O_2 by volume, with N_2 as the equilibrium gas. The gaseous hourly space velocity (GHSV) was set at 30,000 h^{-1}, with a stream time of 30 min for each temperature. The calculation equations of NO conversion, CB

conversion, and the selectively of N_2, HCl, Cl_2, CO, and CO_2 are supplied in the supporting information.

3. Results and discussion

3.1. Catalytic performance

The synergistic catalytic efficiency of CB and NO over different catalysts in the temperature range of 120–300 ℃ is shown in Fig. 1. MnCeOx-SiW exhibited the highest synergistic catalytic activity, followed by MnCeOx, then MnCeOx-PW, and MnCeOx-SiMo. It suggests that the appropriate surface POM structure further optimizes the low-temperature catalytic performance of MnCeOx. Specifically, the POM-SiW structure modification reduces the T_{90} (The required reaction temperature when the conversion rate reaches 90 %) of CB to 167 ℃ and extends the catalytic temperature window for NO conversion (120–210 ℃) in the synergistic catalytic system. Moreover, the CB conversion rate increased with temperature for all catalysts. However, higher temperatures appeared to suppress the NH_3-SCR reaction over MnCeOx-SiW and MnCeOx-PW, resulting in decreased NO conversion rates at elevated temperature. The NO conversion rate of MnCeOx-SiMo initially increased with temperature and then stabilized, though its low-temperature performance was suboptimal. At 180 ℃, the NO and CB conversion rates for MnCeOx-SiMo were 85.4 % of 13.7 %, respectively. In contrast, MnCeOx-SiW achieved nearly complete conversion of both CB and NO at 180 ℃. MnCeOx-PW demonstrated slightly lower CB catalytic performance at 180 ℃, with a conversion rate of 82.2 %. The impact of the loading amount of POM-SiW and high CB concentration on the catalytic performance was further investigated. Study results (Fig. S1) indicate that the catalyst exhibits optimal low-temperature activity for CB oxidation when the precursor loading is 1 %, achieving a T_{90} of 162 ℃. Further increasing the precursor loading leads to a decline in CB catalytic performance. This phenomenon can be attributed to the excessive formation of polyoxometalate (POM) structures at the catalyst interface, which cover active sites and suppress the low-temperature catalytic oxidation of CB. For NO oxidation above 210 ℃, catalytic performance first decreases and then increases with rising precursor loading, likely due to the interplay between acidic sites and active sites. For the effect of high concentration (500 ppm CB), the increase in CB concentration has an inhibitory effect, reducing the conversion rates of CB and NO to 29.2 % and 85.6 % respectively at 180 ℃ (Fig. S2). On the other hand, the function of Mn and Ce were explored (Fig. S3). The results revealed that CeOx exhibited negligible catalytic activity toward CB and NO at 180 ℃. In contrast, MnOx demonstrated conversion rates of 59.7 % for CB and 87.1 % for NO at the same temperature, both significantly lower than those of MnCeOx (~100 % for CB and NO). Consequently, it can be inferred that CeOx predominantly functions as an electron transfer mediator and adsorption site during the catalytic process, thereby synergistically enhancing the catalytic efficiency of the active site (Mn). From the performance summary table of Ce or Mn-based co-catalytic CB and NO in Table S1, it can be seen that the co-catalytic performance of CB and NO in our work is higher than that in other works.

Fig. 1c-1f illustrate the variation in COx, N_2, and HCl selectivity of MnCeOx and MnCeOx-SiW. MnCeOx and MnCeO-SiW achieved high COx (CO + CO_2) selectivity (~99 %) between 210 and 300 ℃. Notably, POM-SiW structure enhanced low-temperature (120–180 ℃) oxidation performance of MnCeOx-SiW, achieving 86.9 % CO_2 selectivity and 1.5 % CO selectivity at 180 ℃. MnCeOx maintained 100 % N_2 selectivity within the temperature range of 120–240 ℃, whereas a negative correlation with temperature was observed between 240 and 300 ℃, culminating in a decline to 69.1 % at 300 ℃. The phenomenon arises from the dual effects induced by high temperatures [21]: on one hand, it promotes the generation of the intermediate product N_2O, while on the

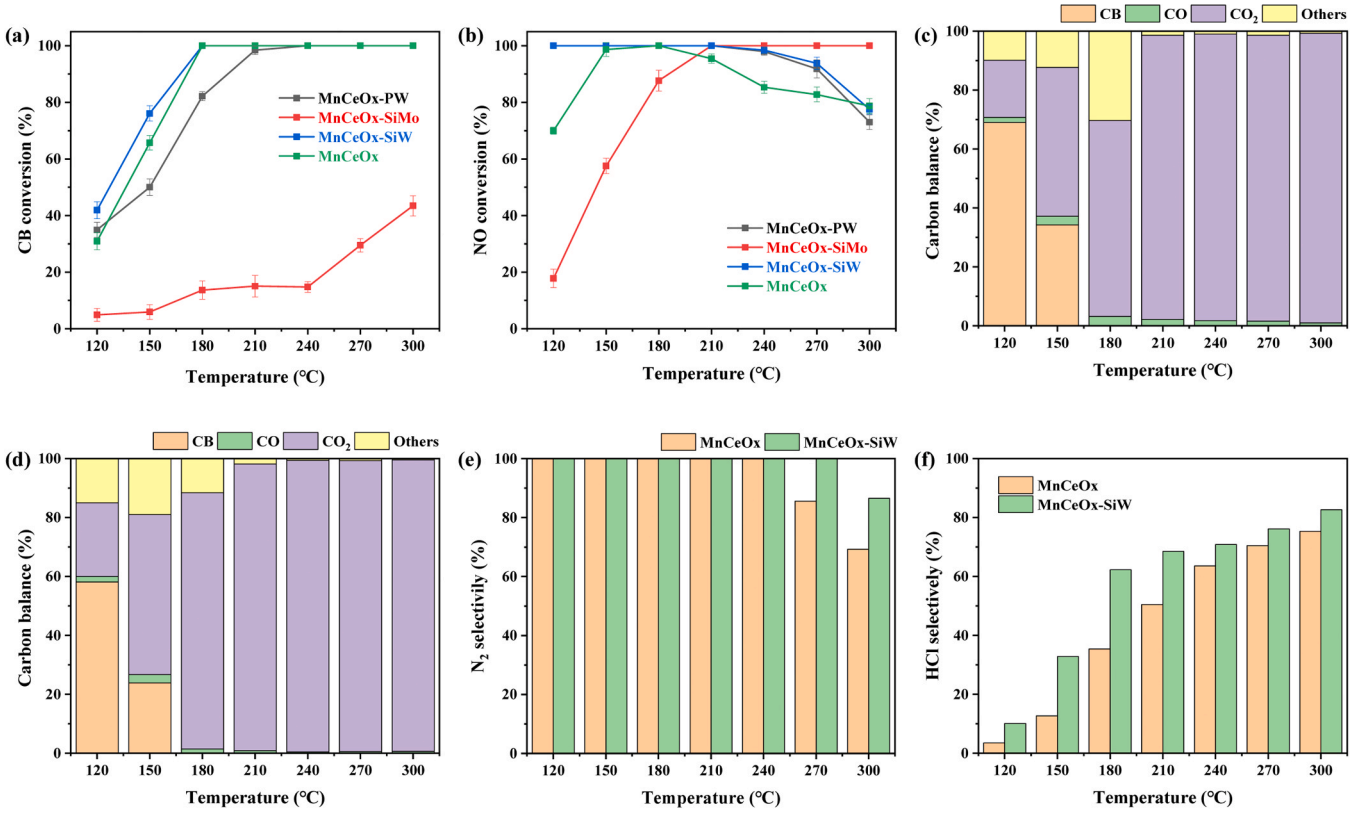

Fig. 1. Synergistic catalytic performance between 120 and 300 ℃ (Conditions: 100 ppm CB, 500 ppm NO, 500 ppm NH_3, 11 vol%O_2, 30,000 h^{-1}), (a) CB conversion, (b) NO conversion, (c) Carbon balance of MnCeOx, (d) Carbon balance of MnCeOx-SiW, (e) HCl selectivity and (f) N_2 selectivity of MnCeOx-SiW and MnCeOx.

other hand, it leads to a reduction in acidic sites on the catalyst surface. For MnCeOx-SiW, its POM-SiW structure achieves a significant enhancement of acidic sites and optimizes the synergistic interaction between acidic sites and redox-active sites. Benefiting from this structural advantage, MnCeOx-SiW exhibits a selective decline in N_2 selectivity (100 % → 86.5 %) only within the 270–300 ℃ high-temperature range. Furthermore, the presence of CB can enhance the selectivity of N_2. This can mainly be attributed to two aspects: below 240 ℃, CB effectively reduces the generation of N_2O; above 240 ℃, CB inhibits the deep oxidation of NH_3 to NO/NO_2 by consuming the reactive oxygen components in the reaction system [22]. The HCl selectivity of MnCeOx and MnCeOx-SiW was lower than the conversion ratios, demonstrating that a portion of chlorine may be deposited on the catalyst surface or participated in chlorinated by-products formation (Fig. 1f). No Cl_2 production was observed at 120–300 ℃. It results revealed that POM-SiW structure facilitates the conversion of organic chlorinated species to inogranic chlorine, and Cl mainly releases in form of HCl.

Fig. S4 illustrate the variation in CB and NO conversion rates over a 400 min reaction period at 180 ℃ for MnCeOx-SiW and MnCeOx, respectively. For CB conversion, both MnCeOx-SiW and MnCeOx initially exhibited high catalytic performance, followed by a decline over time. The NO conversion profile of MnCeOx displayed a similar trend to that of CB conversion. Comparatively, the decline in catalytic performance of MnCeOx-SiW was less pronounced, demonstrating superior synergistic catalytic stability. This can be attributed to the functionalization by POM, which optimizes acidic sites, lattice oxygen, and oxygen vacancies, effectively enhancing NH_3 adsorption and mitigating chlorine poisoning [14]. After 24 h, MnCeOx-SiW retained approximately 90 % CB conversion and complete NO conversion (Fig. 2a-2b). Notably, the presence of H_2O facilitates the formation of hydroxyl radicals on the catalyst surface, thereby enhancing the conversion of NO to NO_2 [23]. Consequently, NO undergoes nearly complete conversion over 24 h in the presence of H_2O. In contrast, H_2O exhibits an inhibitory effect on CB conversion, leading to a decrease in conversion to approximately 70 %. This phenomenon may be attributed to the competitive adsorption of water molecules at the interface, along with their coverage of active sites [24]. To verify the dynamic reversibility of humidity effects, comparative experiments were conducted under high-humidity conditions (20 %) (Fig. S5). Results revealed that excessive moisture decreased the initial CB conversion rate from 91.5 % under dry conditions to 75.5 %, with continued attenuation observed over prolonged reaction time (declining to 63.2 % after 20 h). Notably, CB conversion recovered to 79.2 % upon water vapor removal from the system. Similar trends were observed for NO conversion. It confirms that the H_2O-induced catalytic performance degradation constitutes a reversible process rather than permanent chemical structural breakdown.

To investigate the impact of NO, CB, O_2, and NH_3 on pollutant conversion, the effects were examined by introducing and removing the respective gases, as shown in Fig. 1c-1d. In the system, NO was found to promote CB conversion, while NH_3 exhibited an inhibitory effect on CB conversion. It has been reported that NH_3 and CB undergo competitive adsorption. In the NH_3-SCR reaction, NO is oxidized to NO_2, which facilitates the oxidation of CB and accelerates the redox cycling of the catalyst [25]. Both CB and NH_3 serve as reductants to assist in NO conversion, promoting the forward progression of the NH_3-SCR reaction [26]. Comparatively, NH_3 plays a more significant role in the SCR catalytic system, effectively enhancing NO conversion (from ~48 % to ~96 %), while CB has no noticeable impact on NO conversion in the presence of NH_3. Additionally, oxygen species play a critical role in the catalytic processes of CB and NO. The presence of O_2 in the system replenishes the consumption of oxygen species during the catalytic process, facilitating the regeneration of oxygen vacancies [8]. As a result, both CB and NO conversion rates were significantly enhanced upon O_2 addition (CB conversion: ~23 % → ~97 %, NO conversion: ~17 % → ~95 %), and subsequently decreased after O_2 removal.

3.2. Crystal and chemical structure

The changes in the physicochemical characteristics induced by POM

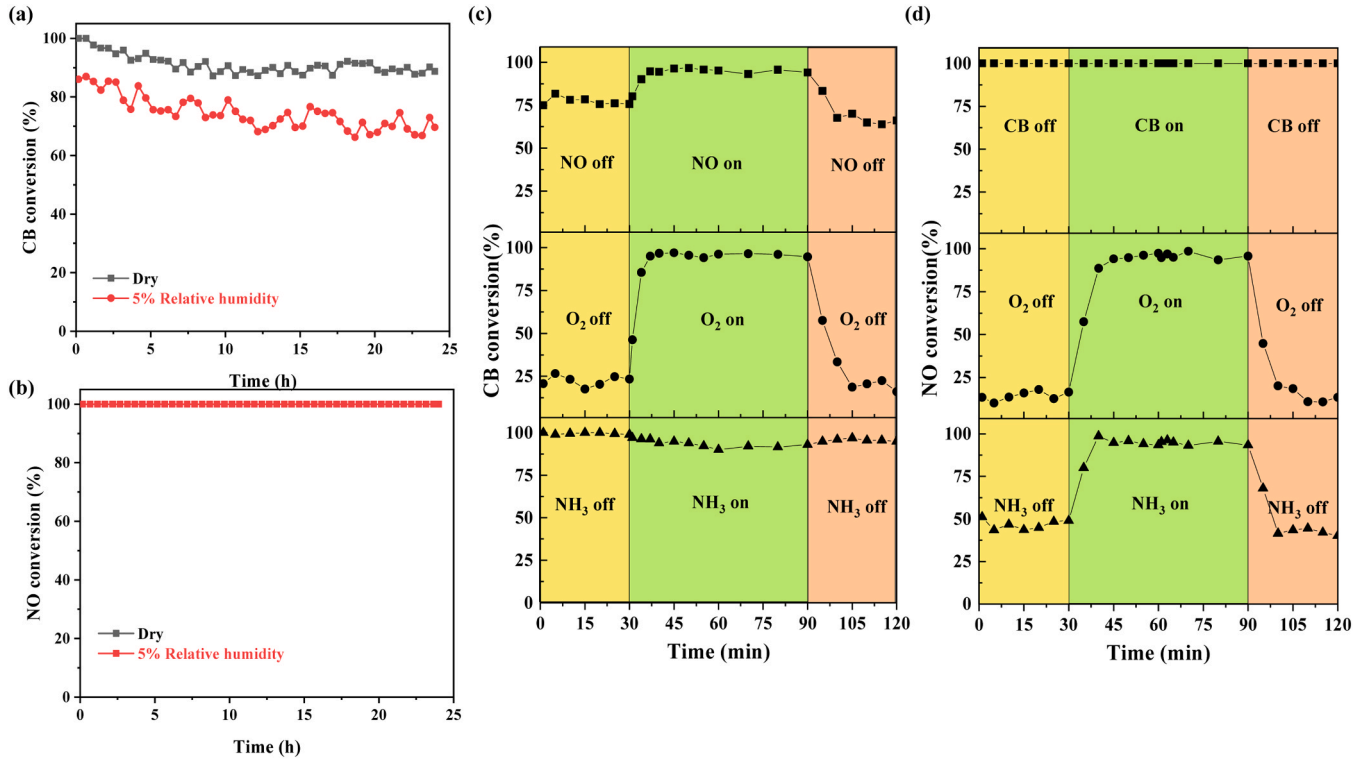

Fig. 2. Catalytic stability of MnCeOx-SiW at 180℃ (Conditions: 100 ppm CB, 500 ppm NO, 500 ppm NH_3, 11 vol%O_2, 30,000 h^{-1}), (a) CB conversion, (b) NO conversion, (c) the impact of NO, O_2, NH_3 in CB conversion, (d) the impact of CB, O_2, NH_3 in NO conversion.

functionalization can be visualized through various characterizations, including XRD, BET, SEM, TEM, and EPR. As shown in Fig. S6a, the MnCeOx sample exhibits an amorphous structure, primarily due to the formation of a MnCe solid solution [27]. The impact of POM precursors (Silicotungstic acid, phosphotungstic acid, and silicomolybdic acid) on the specific surface area and pore structure was investigated via N_2 adsorption isotherms (Fig. S6b and Fig. S6c). Although chemical etching introduces more defects during the preparation process, the formation of the acid-site POM coating leads to a reduction in specific surface area, pore diameter, and pore volume (Table 1). Among these, the MnCeOx-SiW catalyst, with silicotungstic acid as the precursor, exhibits relatively smaller reductions in surface area, pore volume, and pore diameter, which are 91.64 m^2/g, 0.32 cm^3 /g, and 6.2 nm, respectively. This suggests that the POM structure not only formed on the surface but also exists within the pores. According to IUPAC classification, the N_2 adsorption-desorption curves of the samples primarily exhibit a type IV isotherm. The hysteresis loop observed during desorption at low pressure corresponds to the H3 type, indicating that mesopores formed by particle aggregation are the primary pore structure [28].

Fig. 3 shows that all samples consist of relatively uniform particles (~10 nm in size), with a large amount of "amorphous" matrix and randomly distributed crystalline domains can be observed on the surface of the samples. This observation is consistent with the XRD analysis. The abundant amorphous matrix, along with the presence of a large number of oxygen vacancies, can promote the activation of molecular oxygen and the transfer of lattice oxygen. The EPR spectra (Fig. S7) reveal the changes in the uncoordinated electrons at the oxygen vacancy. The electron spin concentration of oxygen vacancies as follows: MnCeOx-SiW (5.87×10^{13} spins/g) > MnCeOx-SiMo (3.64×10^{13} spins/g) > MnCeOx-PW (2.54×10^{13} spins/g) > MnCeOx (1.71×10^{13} spins/g). The increased electron spin concentration confirms that the formation of the surface POM structure facilitates the creation of oxygen vacancies, which in turn promote the migration and transformation of oxygen species [29]. Among these, the POM-SiW structure contributes most significantly to the increase in oxygen vacancy content. Additionally, the uniform distribution of elemental components (Si, P, W, and Mo) on the surface (Fig. S8). It further indicates that the POM structures (POM-PW, POM-SiMo, and POM-SiW) are synthesized on the surface of MnCeOx with, without significantly altering its morphology. The surface atomic Mn/Ce weight ratio of MnCeOx-PW, MnCeOx-SiMo, MnCeOx-SiW, and MnCeOx was 3.40, 4.07, 7.00 and 9.64 comparing to 1.55, 2.16, 1.78, and 2.89 from ICP-OES results, respectively, revealing more Mn on the catalysts surface.

As shown in Fig. 4, the peaks near 640.8 eV, 642.1 eV, 643.6 eV, and 646.1 eV correspond to Mn^{2+}, Mn^{3+}, Mn^{4+}, and Mn^{2+} satellite peak, respectively [29,30]. The Ce 3d spectrum shows 8 deconvolution peaks, which correspond to Ce^{3+} species (v': 885.5 eV, u': 903.6 eV) and Ce^{4+} species (v: 882.6 eV, v'': 889.7 eV, v''': 898.2 eV, u: 901.2 eV, u'': 907.5 eV, u''': 916.6 eV) [30]. Mn^{4+} exhibits strong low-temperature activity for NH_3-SCR and can effectively accelerate the generation of the highly oxidative NO_2, which is favorable for the CB oxidation in the synergistic process. Therefore, the MnCeOx-SiW catalyst, rich in Mn^{4+} on the surface, demonstrates the best low-temperature synergistic catalytic performance. As shown in Table 1, POM functionalization leads to different changes in the Mn and Ce species, which can be attributed to the connection between Mn and Ce (Mn-O-Ce), allowing interaction through bridging oxygen ($Ce^{3+} + Mn^{3+/4+} \rightarrow Ce^{4+} + Mn^{2+/3+}$). The surface POM-SiW structure effectively increases the Mn^{4+} (37.3 % → 39.4 %) and Ce^{3+} (20.4 % → 21.4 %) content, while POM-SiMo and POM-PW show the opposite trend, consistent with their catalytic performance.

Table 1
Physical and chemical properties of catalyst.

Sample	S_{BET}[a] (m^2/g)	V_p[b] (cm^3/g)	D_p[c] (nm)	Mn/Ce[d] (wt%)	Mn/Ce[e] (wt%)	Mn^{4+}/Ce^{3+}[f] (%)	O_{lat}/O_{ads}[f]
MnCeOx-PW	87.34	0.19	7.0	3.40	1.55	31.3/19.4	1.8
MnCeOx-SiMo	89.26	0.21	7.5	4.07	2.16	28.4/12.3	1.6
MnCeOx-SiW	91.64	0.32	6.2	7.00	1.78	39.4/21.4	2.1
MnCeOx	94.22	0.37	11.96	9.64	2.89	37.3/20.4	1.5

[a] Surface Area.
[b] Desorption cumulative volume of pores.
[c] Desorption average pore diameter.
[d] The ratio of Mn and Ce obtained from SEM-EDS results
[e] From ICP-OES results.
[f] From XPS results.

The peaks at 529.6 eV, 531.6 eV, and 533.4 eV correspond to lattice oxygen (O_{lat}), adsorbed oxygen (O_{ads}), and hydroxyl oxygen (O_{wat}) [27,29]. The POM functionalization on the catalyst surface effectively activates O_{lat}, causing it to shift to a lower binding energy (529.3 eV). The O_{lat}/O_{ads} ratio follows the order: MnCeOx-SiW (2.1) > MnCeOx-PW (1.8) > MnCeOx-SiMo (1.6) > MnCeOx (1.5), indicating that the surface POM structure primarily connects through O_{lat} as a bridge, and it lead to a significant increase in O_{lat} content after POM functionalization [14]. Simultaneously, the consumption of O_{lat} promotes the formation of oxygen vacancies, which is consistent with the EPR results. The O_2-TPD curve is used to evaluate the oxygen storage capacity (Fig. 4d). The oxygen desorption peaks in the temperature ranges of 50–300 ℃, 300–500 ℃, and 500–700 ℃, corresponding to adsorbed oxygen, surface lattice oxygen, and bulk lattice oxygen, respectively [31]. No bulk lattice oxygen peaks are observed in the MnCeOx spectrum, primarily because their desorption temperature exceeds 700℃. The strong interaction between the surface POM structure and MnCeOx promotes the migration of bulk lattice oxygen to the surface, effectively lowering the activation temperature of bulk lattice oxygen [32]. The desorption temperature of surface adsorbed oxygen for MnCeOx-SiW (237 ℃) is lower than that of MnCeOx-SiMo (240 ℃) and MnCeOx-PW (254 ℃), indicating that the surface adsorbed oxygen in MnCeOx-SiW is more easily migrated and converted. On the other hand, the removal of NOx is closely related to the reducibility of the catalyst. The H_2-TPR spectrum (Fig. 4e) shows two reduction peaks in the temperature range of 100–550 ℃, which are attributed to the reduction of O_{ads} and O_{lat} [33]. After POM functionalization, the reduction temperature of O_{lat} in MnCeOx-SiMo shifts to higher temperatures, whereas MnCeOx-SiW and MnCeOx-PW shifts to lower temperatures. It suggested that the formation of interfacial POM-SiW and POM-PW structures could enhance the catalyst's reducibility, consequently lowering the operational temperature for lattice oxygen involvement in the NH_3-SCR reaction. It corresponds to the activity test results of NO.

3.3. Electronic structure

The Mn as the active site for low-temperature reactions in MnCeOx. To further investigate the impact of POM functionalization on the active sites of MnCeOx, X-ray absorption near-edge structure (XANES) and extended X-ray absorption fine structure (EXAFS) analyses were conducted. Fig. 5a shows the Mn K-edge XANES spectra for MnCeOx and MnCeOx-SiW. After POM functionalization, the absorption edge of MnCeOx shifts to higher energies, and the intensity of the white line peak significantly decreases. This indicates that POM functionalization increases the oxidation state of Mn, enhancing the splitting of the 1 s orbital into the 4p orbital. Additionally, the XANES spectra are similar to the Mn_3O_4 reported [34], suggesting that Mn in MnCeOx predominantly exists in the form of Mn_3O_4. The Mn K-edge EXAFS oscillation function $k^2\chi(k)$ (Fig. S9) shows similar oscillatory structures for MnCeOx and MnCeOx-SiW. Fig. 5b displays the Mn K-edge of the Fourier transform in R-space, weighted by $k^3[\chi(k)]$. The peaks around 1.5 Å and 2.5 Å are attributed to Mn-O and Mn-Mn interactions [35]. Additionally, no Mn-Ce, Mn-Si, or Mn-W scattering is observed. It could be attributed to

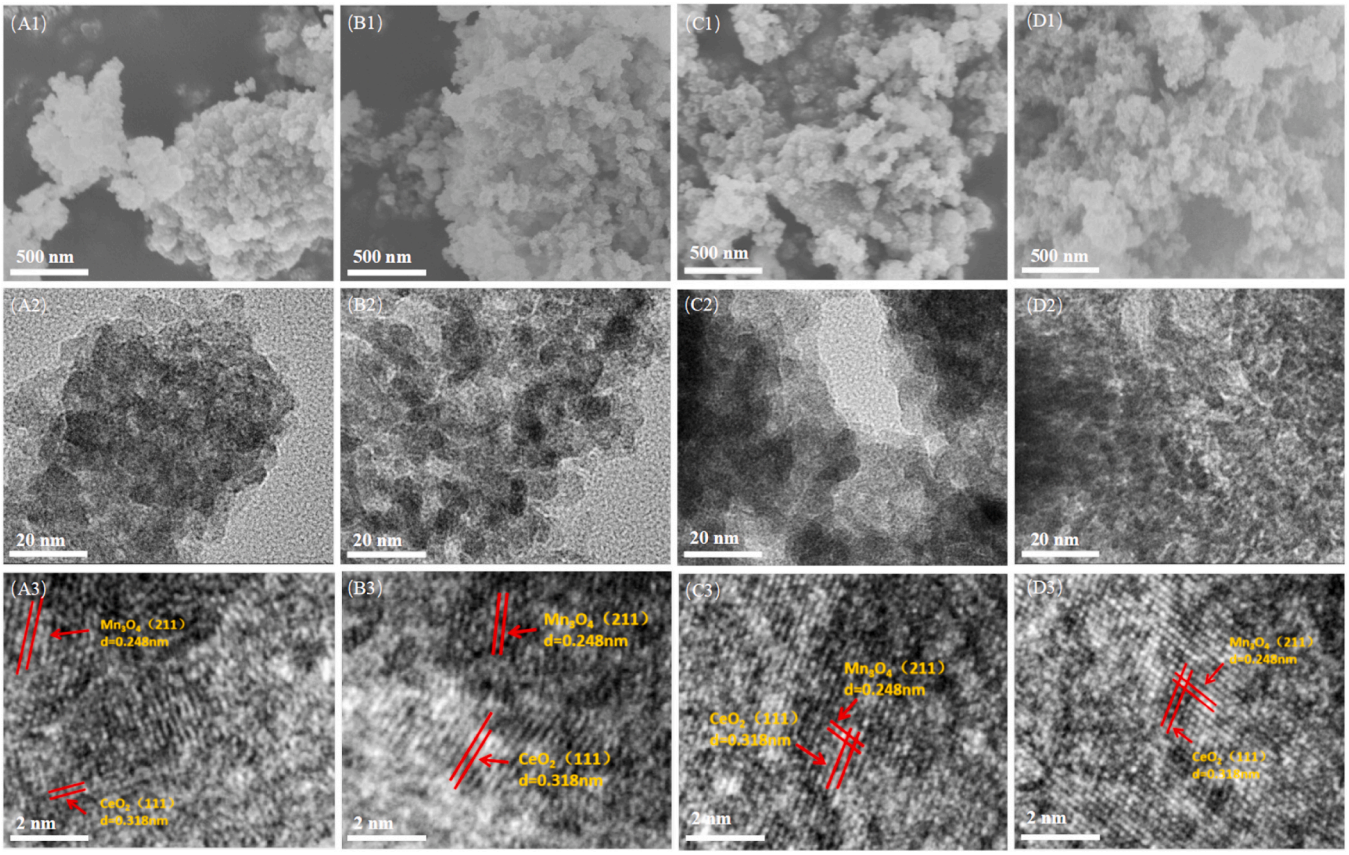

Fig. 3. SEM and HRTEM images of (A1-A3) MnCeOx-PW, (B1-B3) MnCeOx-SiMo, (C1-C3) MnCeOx-SiW, and (D1-D3) MnCeOx.

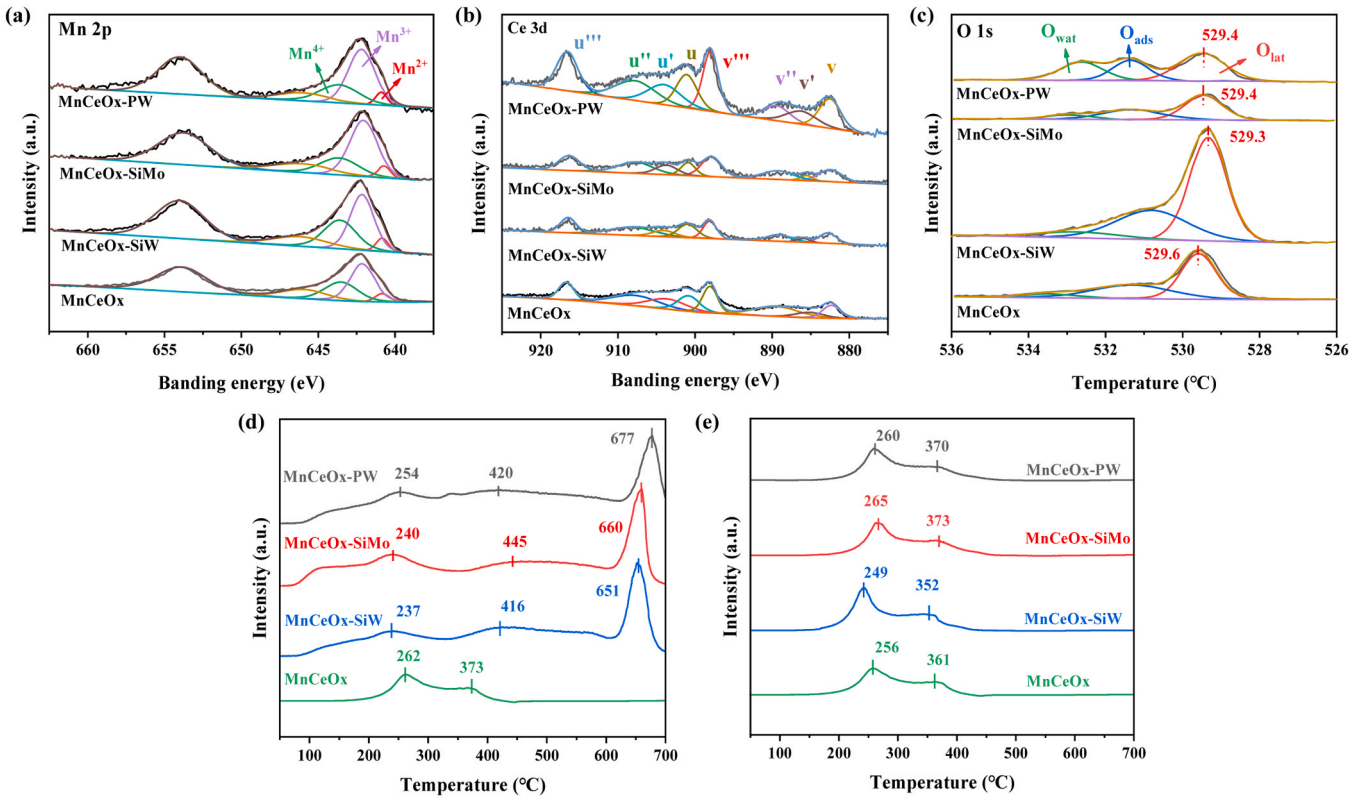

Fig. 4. (a) XPS Mn 2p spectra, (b) XPS Ce 3d spectra, (c) XPS O 1 s spectra, (d) O_2-TPD profils, (e) H_2-TPR profiles.

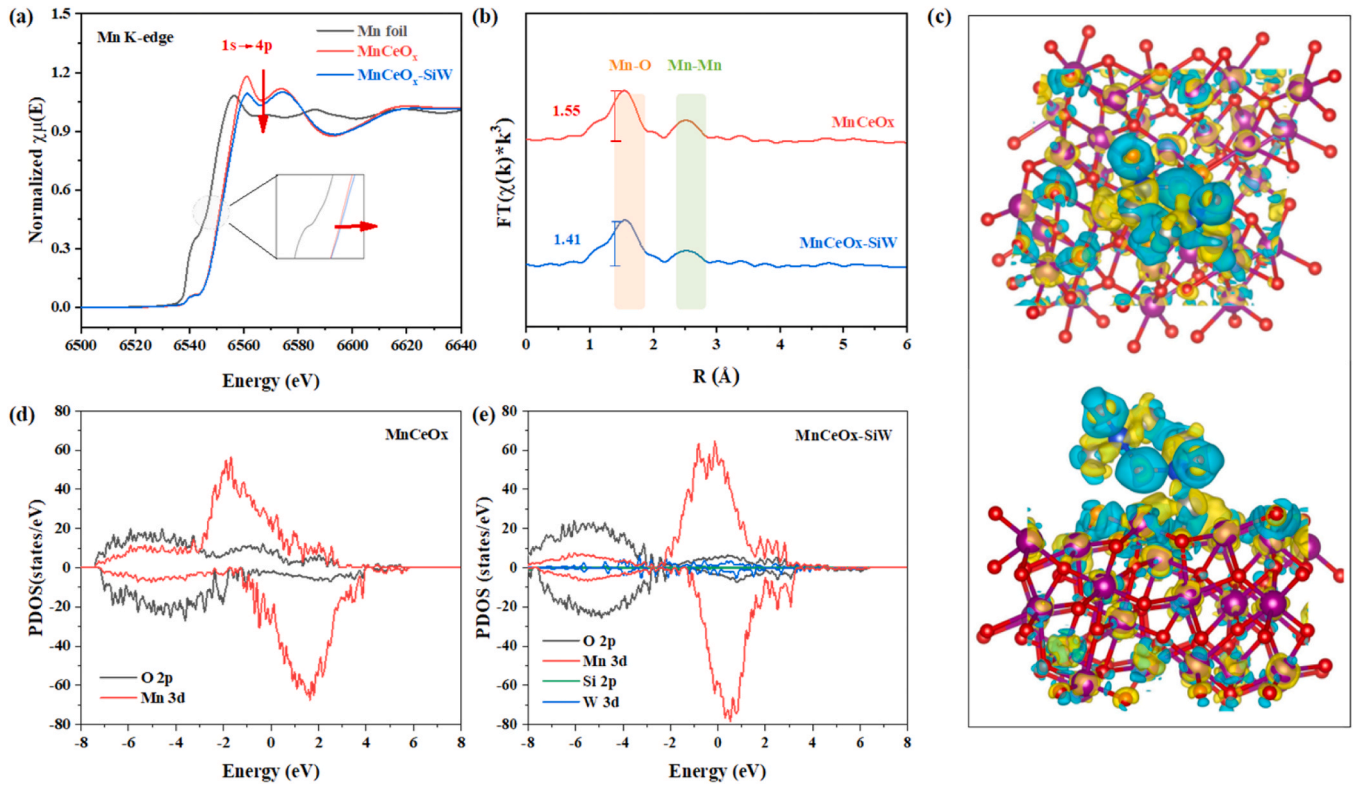

Fig. 5. (a) Mn K-edge XANES spectra; insets are magnified absorption edge and the White line intensity, (b) FT-EXAFS spectrum for the Mn K-edge, (c) differential charge diagram of MnCeOx-SiW, (The red, purple, blue, silver represent O, Mn, W, and Si atoms, respectively), PDOS of (d) MnCeOx and (e) MnCeOx-SiW.

Ce predominantly coordinating through Ce-O, while the atomic content of Si and W is relatively low. As demonstrated in Table S2, the elongation of Mn-O bond length (1.90 → 1.91 Å) in the MnCeOx-SiW structure indicates a reduction in bond energy, which effectively enhances dynamic electron cycling between Mn^{4+} and Ce^{3+}. This phenomenon exhibits a synergistic effect with the characteristic shift in lattice oxygen binding energy (529.6 → 529.3 eV) observed in MnCeOx-SiW. The coordinated mechanism accelerates the regeneration of surface active oxygen species while establishing an efficient Mn^{4+}-O-Ce^{3+} charge compensation pathway through metal-oxygen interactions, thereby achieving enhanced catalytic efficiency.

To further confirm the effect of POM grafting on the coordination structure of MnCeOx-SiW, wavelet transform (WT) of the Mn K-edge EXAFS oscillations was performed (Fig. S10). The two strongest peaks, associated with the Mn-O and Mn-Mn coordination paths, show a decrease after POM functionalization. The XAFS results clearly indicate that, although the initial structures are similar, the irreversible local reconstruction of electron is a direct structural response of the catalyst to POM functionalization, reflecting an alteration in the catalyst's microstructure.

To investigate the effect of POM-SiW structure on the surface electronic structure of active site (Mn_3O_4), a coupling model of Mn_3O_4-SiW was established using the Mn_3O_4 (211) crystal face as the active facet and the $Si_4W_2O_3$ as the POM-SiW structure. The local charge density difference was calculated, as shown in Fig. 5c. Due to the interface coupling between Mn_3O_4 and $Si_4W_2O_3$, the charge density of surface oxygen atoms on Mn_3O_4 significantly increases, while the charge density of adjacent Si atoms decreases. It suggests that electrons transfer from the interface Si in $Si_4W_2O_3$ to the O atoms in Mn_3O_4, which could activate the O_{lat} in Mn_3O_4 [36]. To confirm this, the projected density of states (PDOS) was analyzed to elucidate the interaction between orbitals (Figs. 5d-4e). The introduction of $Si_4W_2O_3$ widens the band gap, increasing the electron occupancy and splitting of the O 2p orbital states, while electrons from the Mn d orbitals are transferred to unoccupied states. This indicates that $Si_4W_2O_3$ suppresses the transfer of electrons from the O 2p orbitals to the empty Mn 3d orbitals, thereby weakening the Mn-O bond [20].

3.4. The role of acid sites

Surface acidic sites play a critical role in catalytic processes and have a significant impact on low-temperature catalytic stability. NH_3-temperature programmed reduction (NH_3-TPD) analysis was used to investigate the acidity of samples. The results show that the surface acidity of catalysts consists of weak acid sites (50–200 ℃), moderate acid sites (200–350 ℃), and strong acid sites (>350 ℃) (Fig. 6a) [37]. The significant increase in acid content after POM functionalization is mainly attributed to the precursor etching during the preparation process (Table S3). Notably, MnCeOx-SiW exhibited lower desorption temperatures for weak acidic (108 ℃) and moderate acidic sites (247 ℃), indicating that MnCeOx-SiW is more readily involved in NH_3 adsorption and desorption at low temperatures, thereby facilitating NO conversion. To identify the surface acidity of the samples, pyridine infrared (Py-IR) spectroscopy was used to determine the types and quantities of acidic sites on the catalyst surface (Fig. 6b and Fig. S11). The peaks at 1440 cm^{-1} and 1575 cm^{-1} are attributed to the molecular in-plane ring deformation vibration of pyridine adsorbed on weak Lewis acid sites on the catalyst surface. The peak at 1605 cm^{-1} corresponds to strong Lewis acid sites, the peak at 1530 cm^{-1} is associated with Brønsted acid sites. The vibration peak at 1488 cm^{-1} is attributed to the synergistic peak of Lewis and Brønsted acid sites [38]. Quantitative analysis of the Lewis and Brønsted acid sites reveals that POM functionalization could significantly enhances surface acidity sites. Among the samples, MnCeOx-SiW has the highest number of acidic sites. However, as the temperature increases, the number of Lewis acid sites decreases significantly, resulting in a higher Brønsted/Lewis ratio. Combined with analysis of carbon balance and N_2 selectivity (Fig. 1), the information could be inferred that weak acid sites dominate the CO

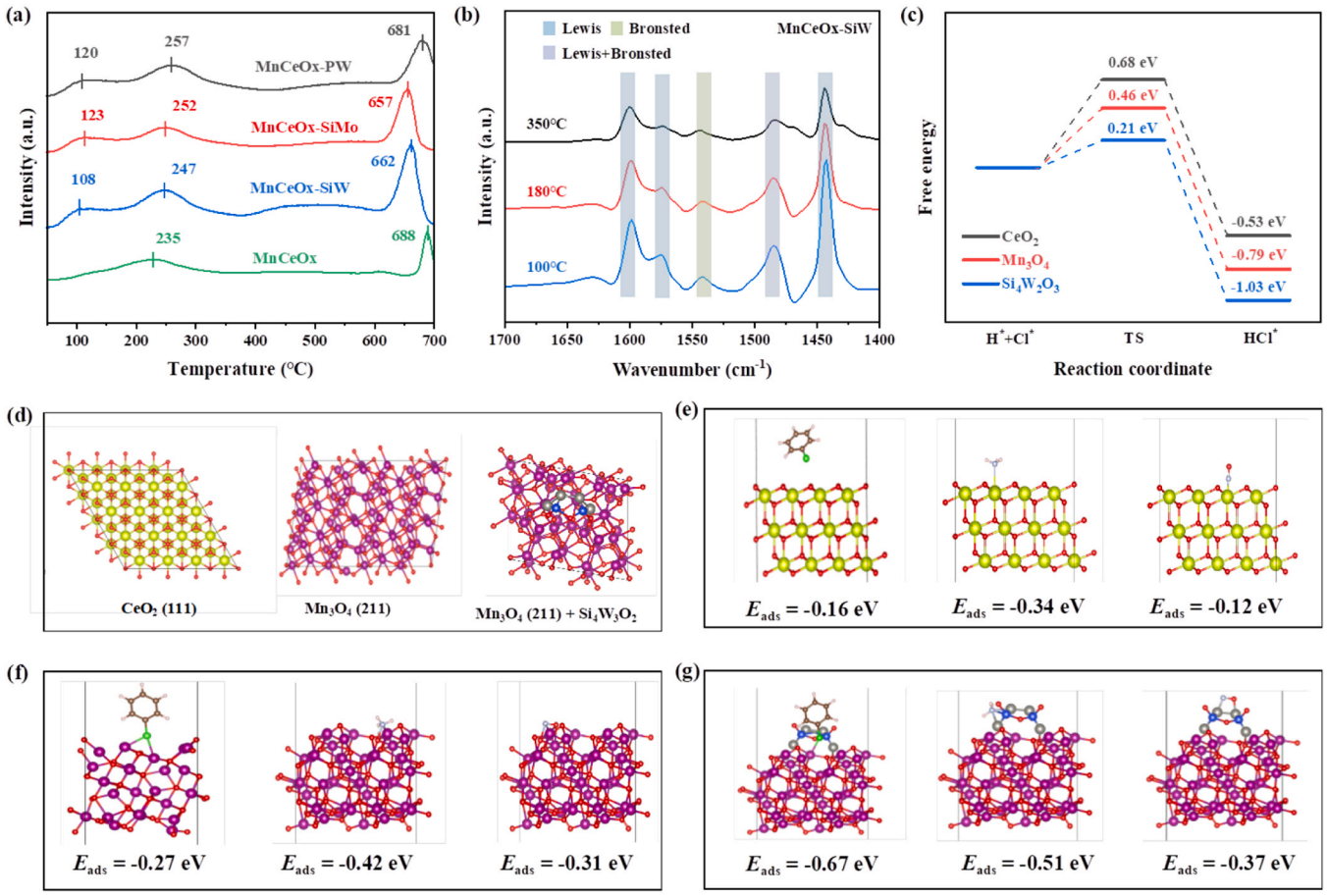

Fig. 6. (a) NH_3-TPD profiles, (b) Py-IR spectra of MnCeOx-SiW, (c) Free-energy profiles of the HCl formation pathways on CeO_2 (111), Mn_3O_4 (211) and Mn_3O_4 (211)-$Si_4W_2O_3$, (d) Crystal structure of CeO_2 (111), Mn_3O_4 (211) and Mn_3O_4 (211)-$Si_4W_2O_3$, (e-g) CB, NH_3, and NO adsorption configurations of CeO_2 (111), Mn_3O_4 (211) and Mn_3O_4 (211)-$Si_4W_2O_3$. (The Green, pink, red, silver, grey, blue, purple and yellow represent chlorine, hydrogen, oxygen, nitrogen, silicon, tungsten, manganese and cerium atoms, respectively).

oxidation pathway at low temperatures (120–180 ℃), achieving 86.9 % CO_2 selectivity at 180 °C. In contrast, Brønsted acid sites at elevated temperatures (270–300 ℃) enhance N_2 selectivity by activating nitrogen-containing intermediates, reaching 100 % at 270 ℃. Furthermore, Furthermore, acid sites with higher strength promote HCl formation, inhibits the electrophilic chlorination of CB, and makes the HCl selectivity of MnCeOx-SiW (62.3 %) higher than that of MnCeOx (35.4 %) at 180 ℃ [39,40].

The formation of Cl-containing species is one of the key factors influencing the stability differences among catalysts. The formation energy of HCl on the POM-SiW structure (0.21 eV) is lower than that on Mn_3O_4 (0.46 eV) and CeO_2 (0.68 eV) (Fig. 6c). It can be inferred that Mn_3O_4 is the main dechlorination site of MnCeOx, the combination of POM-SiW and Mn_3O_4 facilitates the dechlorination of CB on the POM-SiW phase and the subsequent formation of HCl, thereby preventing chlorine poisoning of the active sites (Mn_3O_4). Adsorption models of CB, NO, and NH_3 on Mn_3O_4-SiW, Mn_3O_4, and CeO_2 were constructed (Fig. 6d-6g). The results indicate that NH_3 preferentially adsorbs on Mn_3O_4 and CeO_2 surfaces, whereas NO and CB may undergo competitive adsorption in the system. Based on adsorption energy calculations, CeO_2 exhibits the weakest adsorption capacity for CB, NO, and NH_3. The formation of the POM-SiW structure on Mn_3O_4 enhances its adsorption capacity, resulting in a stepwise adsorption order sequence for CB (|-0.67 eV|), NH_3 (|-0.51 eV|), and NO (|-0.37 eV|), thereby suppressing competitive adsorption. Consequently, Mn_3O_4-SiW is presumed to primarily function as a CB adsorption site in the initial reaction stage, while the neighboring acidic sites effectively adsorb NH_3, promoting NH_4Cl formation and accelerating chloride ion dissociation. The finding is consistent with the stability tests and TOF-SIMS characterization results (Fig. S12).

3.5. Synergistic catalytic mechanism

In situ DRIFTs, and TOF-SIMS analyses were conducted to investigate the interfacial reactions and catalytic pathways. As shown in Fig. 7, the bands at 1399, 1486, and 1592 cm^{-1} are attributed to the in-plane skeletal vibrations of the aromatic ring in CB (Table 2) [41]. The absorption band at 1303 cm^{-1} corresponds to phenolate species, while the peak at 1685 cm^{-1} is assigned to quinone [32]. The bands at 2340 and 2356 cm^{-1} are attributed to CO_2 [29]. According to the results of TOF-SIMs, it can be seen that intermediate products such as chlorine atoms, benzene, phenol, quinone, maleic anhydride, and acetic acid continuously deposit on the catalyst surface over time (Fig. 7b). Therefore, the information can be inferred that CB primarily follows the LH mechanism. CB is adsorbed onto the Lewis acid sites, and then undergoes a nucleophilic substitution reaction at the active sites with the participation of reactive oxygen species, resulting in the formation of intermediate products such as phenol and quinone, as well as final products like CO, CO_2, and H_2O. Meanwhile, the peaks at 1060 and 1507 cm^{-1} assigned to monodentate nitrate are observed. The peak at 1240 cm^{-1} corresponds to bridging nitrate [32]. The peaks at 1433 and 1625 cm^{-1} are considered to be associated with the Bronsted-acid adsorbed NH_4^+ (B-NH_4^+) and Lewis-acid adsorbed NH_3 (L-NH_3), respectively [42]. The peaks at 1345 and 1541 cm^{-1} are attributed to the inert

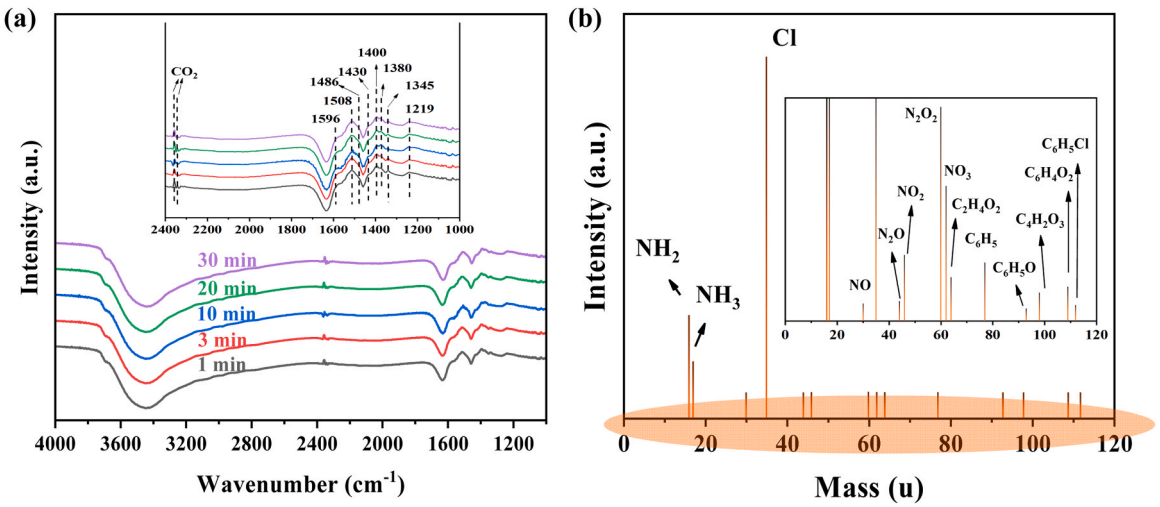

Fig. 7. (a) In-situ DRIFTs spectra of surface functional groups changes with time on MnCeOx-SiW (Conditions: 500 ppm NO, 500 ppm NH_3, 100 ppm CB, 11 vol% O_2), (b) the sediment ions in nepositive (-) for post-reaction MnCeOx-SiW.

Table 2
The species information of in-situ DRIFT spectra.

Wavenumbers (cm^{-1})	Species
1240	Bridging nitrates
1303	Phenate
1345	$N_2O_2^{2-}$
1433	B-NH_4+
1060, 1507	Monodentate nitrites
1399, 1486, 1592	Aromatic ring
1541	-NH_2
1625	L-NH_3
1675	benzoquinone
2321, 2356	CO_2

$N_2O_2^{2-}$ and -NH_2 species [32,43]. These substances correspond to NH_2, NH_3, NH, NO_3^-, $N_2O_2^{2-}$, and other species observed in the TOF-SIMS results. Therefore, it can be inferred that NH_3 is adsorbed at the acidic sites (mainly via Lewis acid adsorption) during the catalytic process, existing in the forms of NH_{3ads} and NH_4^+. NH_{3ads} or NH_4^+ breaks and forms, $N\text{-}NHOH_{ads}$, $N\text{-}NOH_{ads}$, N_2O, N_2, and H_2O under the attack of active oxygen species, while the hydrogen atoms are captured by the catalyst surface, leading to the regeneration of consumed Brønsted acidic sites or release of HCl [5]. In addition, a decrease in the species of $N_2O_2^{2-}$ (1344 cm^{-1}), B-NH_4^+ (1418 cm^{-1}), Monodentate nitrites (1511 cm^{-1}) were observed with the temperature increase (150 → 210 ℃) on the catalyst surface, while the amounts of Aromatic ring (1399, 1490, 1595 cm^{-1}) and phenate (1303 cm^{-1}) increase (Fig. S13). It further confirmed that an increase of temperature results in a decrease content of acidic sites and enhanced catalytic activity for CB, suppress the NH_3-SCR reaction.

To further investigate the impact of POM functionalization on the catalytic pathway, in-situ DRIFTs spectra of MnCeOx and MnCeOx-SiW were compared, as shown in Fig. S14. Compared to MnCeOx, the surface concentrations of nitrogen-containing species were increased after POM functionalization, such as monodentate nitrates (1507 cm^{-1}), bridged nitrates (1240 cm^{-1}), and B-NH_3 (1433 cm^{-1}), as well as the content of the benzene ring (1380, 1490 cm^{-1}). Furthermore, the surface concentrations of deposited species such as Cl^-, $C_6H_5Cl^-$, $C_4H_2O_3^-$, NO_3^-, and $N_2O_2^{2-}$ on MnCeOx-SiW exhibit a decreasing trend, while intermediate products including phenol (C_6H_6O), quinone ($C_6H_4O_2$), acetic acid ($C_2H_4O_2$), NO_2, N_2O, NH_4Cl, and adsorbed species (NO, NH_3, and NH_4) show a increase (Fig. S12). It indicates that POM functionalization effectively enhances the conversion rates of CB, NO, and NH_3, as well as a higher number of acidic sites and promote the dissociation of the Cl atom in CB and the formation of NH_4Cl [25].

To further investigate the synergistic mechanism between CB and NO, the effects of different atmospheres on the interfacial reactions were studied. The impact of CB on the NH_3-SCR reaction is displayed in Fig. 8a. At the early stage of the reaction, bridging nitrate (1252 cm^{-1}), $N_2O_2^{2-}$ (1348 cm^{-1}), monodentate nitrate (1506 cm^{-1}), and L-NH_3 (1620 cm^{-1}) can be observed. The species on the catalyst surface gradually increase over time until saturation is reached. As for the B-NH_4^+, it only observed at the reaction initial, indicating that NH_4^+ is rapidly consumed at the beginning. Compared to the NH_3-SCR reaction alone, the introduction of CB leads to the appearance of vibration peaks corresponding to adsorbed aromatic rings (1399, 1482, 1592 cm^{-1}), benzquinone (1676 cm^{-1}), B-NH_4^+ (1433 cm^{-1}), inert $N_2O_2^{2-}$ (1348 cm^{-1}), and -NH_2 (1541 cm^{-1}) on the surface. These peaks gradually intensify over time, while the L-NH_3 (1620 cm^{-1}) and bridging nitrate (1252 cm^{-1}) peaks show the opposite trend. It suggests that the addition of CB can effectively accelerates the electron transfer rate, enhancing the conversion of NH_3 to NH_4^+ and promoting the formation of NH_2 and $N_2O_2^{2-}$, which in turn inhibits the deposition of bridging nitrates. Moreover, no open-ring products (maleic anhydride, acetate salts) were observed, which could be attributed to the coverage by nitrogen-containing functional groups. The NH_3 and O_2 impacts was analyzed in the synergistic catalytic system. As Fig. 8b displayed, the intensity of the functional group peaks on the catalyst surface gradually increased from 0 to 30 min. However, there were no significant changes in the surface functional groups or their peak intensities after the addition of NH_3, suggesting NH_3 can accelerate the redox reactions and reduce the deposition of carbon- or nitrogen-containing species. The addition of O_2 have a great influence on the surface functional groups, as shown in Fig. 8c. During the initial 30 min reaction, the intensity of the functional group peaks on the catalyst surface (e.g., quinone at 1675 cm^{-1}, $N_2O_2^{2-}$ at 1349 cm^{-1}, aromatic ring at 1405 cm^{-1}, and L-NH_3 at 1626 cm^{-1}) gradually increased over time under anaerobic conditions. However, the NH_2 functional group exhibited a different trend, with an initial increase followed by a decrease. Hence, it can be inferred that O_{lat} determines the formation rate of NH_2. Additionally, bridging nitrate (1240 cm^{-1}) appears upon the introduction of O_2. The peak intensities of NH_2, L-NH_3, and the benzene ring significantly increase over time, while the peak corresponding to benzquinone gradually disappears. It indicates that oxygen species are critical in the NH_3-SCR and CB catalytic processes. The introduction of O_2 effectively replenishes the consumed oxygen species in the system, thereby accelerating the interface reaction rate.

The samples were analyzed for their crystal structure, morphology,

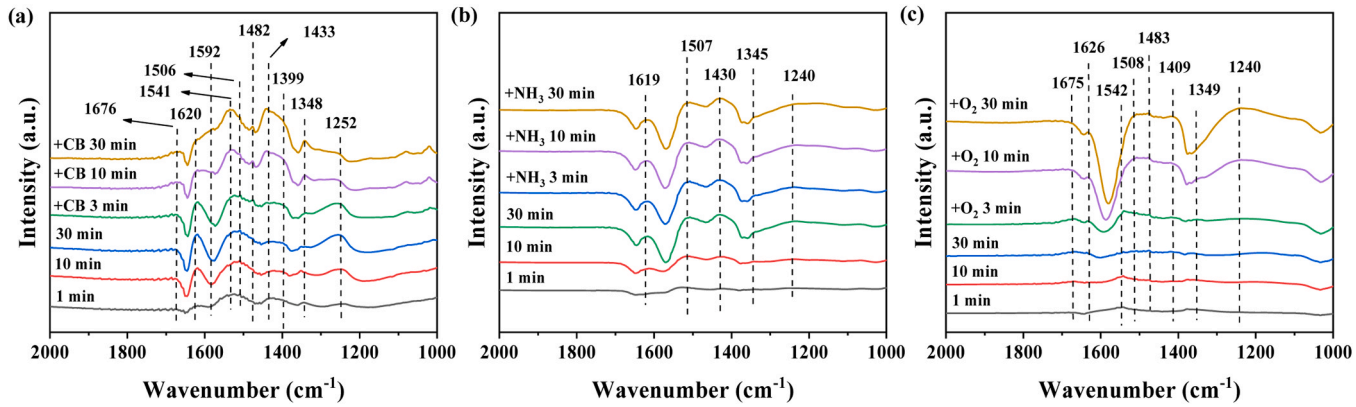

Fig. 8. In-situ DRIFT spectra of surface functional groups changes with gas component, (a) CB impact (Conditions: 500 ppm NO, 500 ppm NH_3, 11 vol% O_2, the addition of 100 ppm CB after 30 min), (b) NH_3 impact (Conditions: 500 ppm NO, 100 ppm CB, 11 vol% O_2, the addition of 500 ppm NH_3 after 30 min), (c) O_2 impact (Conditions: 500 ppm NO, 500 ppm NH_3, 100 ppm CB, the addition of 11 vol% O_2 after 30 min).

and surface element valence states before and after the experiment, with the relevant results shown in Fig. S15-S18 and Table S4. No significant morphological deformation or phase transformation was observed before and after the experiment (Fig. S15-S16). The D_p increased to 12.9 nm after the reaction, indicating that the pore structure was disrupted during the reaction, leading to a decrease in specific surface area and pore volume from 91.64 m^2/g and 0.32 cm^3/g to 90.86 m^2/g and 0.18 cm^3/g, respectively (Fig. S17). It can be attributed to chlorine and carbon deposition on the surface and pores of sample. Higher concentrations of NO and NH_3 effectively promoted the electron cycling ($\equiv Mn^{3+/4+} + \equiv Ce^{3+} \rightarrow \equiv Mn^{2+/3+} + \equiv Ce^{4+}$), resulting in a reduction of Mn^{4+} and Ce^{3+} in the sample after the reaction (Fig. S18). The increase in the O_{ads}/O_{lat} ratio suggests that surface oxygen species participates in the reaction. Notably, the O_{ads}/O_{lat} ratios of MnCeOx-SiW is higher than MnCeOx after the reaction. It further indicates that POM functionalization activates O_{lat}, accelerates its release, and effectively enhances the conversion of active oxygen species in the system. As for the Ce, it primarily exists in the form of an electron transfer mediator.

In summary, a low-temperature synergistic catalytic mechanism for CB and NO is proposed, as illustrated in Fig. 9. CB and NH_3 compete for adsorption at the acidic sites. The NH_3-SCR reaction follows a coexistence mechanism of Langmuir–Hinshelwood (LH) and Eley–Rideal (ER), with the LH mechanism being dominant. Initially, NH_3 is adsorbed on the Lewis and Bronsted acidic sites of the catalyst, forming NH_{3ads} and NH_4^+. Under the function of active oxygen species and active sites, NH_{3ads}/NH_4^+ and NO sequentially form N-$NHOH_{ads}$, N-NOH_{ads}, N_2O, N_2, and H_2O. The $Mn^{2+/3+}$ species, which result from charge transfer and act as active sites. It works synergistically with NO_2, O_{lat}, or nearby O_{ads}, facilitating the rapid oxidation of CB and leading to the formation of intermediate products such as quinone, maleic anhydride, and propionic acid, and even CO, CO_2, and H_2O. On the other hand, the charge compensation for $Mn^{2+/3+} \rightleftharpoons Mn^{3+/4+}$ is mainly provided by $Ce^{4+} \rightleftharpoons Ce^{3+}$. During the initial stage of the NH_3-SCR reaction, NH_4^+ formed acts as a dechlorination agent, facilitating the dissociation of the Cl atom in CB. The Cl atom either combines with another Cl atom or migrates to the Bronsted acidic site, eventually desorbing as Cl_2 or HCl.

4. Conclusion

This study provides an in-depth exploration into the role of POM functionalization in the synergistic catalysis of CB and NO. The proton-conductive POM-SiW framework suppresses chlorine deposition, preventing active-site poisoning, while its electron transfer to lattice oxygen weakens Mn-O bonds and activates lattice oxygen. Furthermore, POM-SiW optimizes surface interactions by mitigating competitive adsorption between reactants and balancing acidity-redox properties, which results in a reduction of the T_{90} for CB to 167 ℃ and an expansion of the NO catalytic temperature window (120–210 ℃) in the synergistic catalytic system. NO_2 and NH_4^+ act as auxiliary oxidants and dechlorinating agents, respectively, synergistically promoting CB decomposition. These insights establish a strategy for lattice oxygen activation, expanding the operational temperature window for the simultaneous control of multiple pollutants (NOx and Cl-VOCs).

CRediT authorship contribution statement

Xuanhao Guo: Writing – original draft, Validation, Methodology. **Shengyong Lu:** Methodology, Conceptualization. **Zhengdong Han:** Writing – review & editing. **Xinlei Xu:** Writing – review & editing, Validation, Data curation. **Guanjie Wang:** Writing – review & editing,

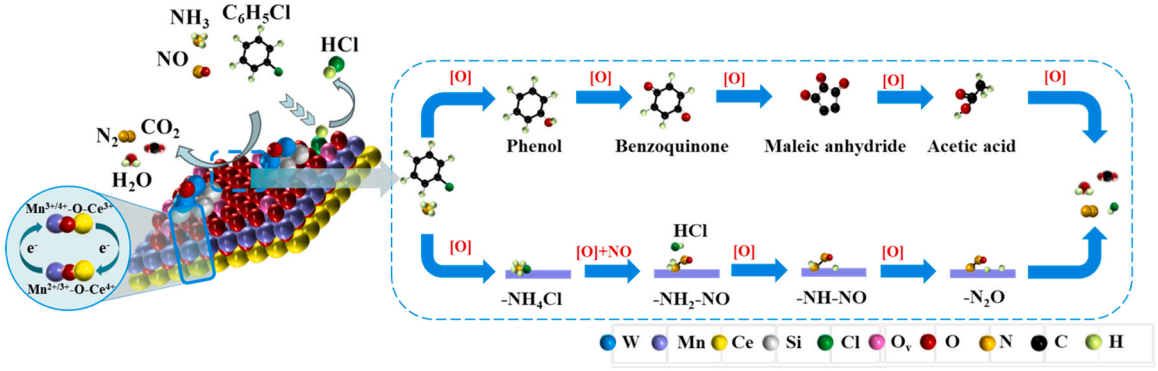

Fig. 9. Possible catalytic mechanism of CB and NO.

Supervision, Funding acquisition. **Min Chen:** Formal analysis. **Yaqi Peng:** Formal analysis. **Beilong Lin:** Formal analysis.

Declaration of Competing Interest

The authors declare that they have no known competing financial interests or personal relationships that could have appeared to influence the work reported in this paper.

Acknowledgments

This work was supported by the “Pioneer” and “Leading Goose” R&D Program of Zhejiang (2023C03125), Zhejiang Province Postdoctoral Science Foundation (ZJ2024106), Science and Technology Plan Project of Taizhou (24sfa02), and National Natural Science Foundation of China (52206176). The authors extend their gratitude to Wang Meifang from Shiyanjia Lab (www.shiyanjia.com) for providing invaluable assistance with the In-situ DRIFTS analysis. The authors would like to thank Qian Wang from SC-GO (www.sci-go.com) for the XPS analysis.

Appendix A. Supporting information

Supplementary data associated with this article can be found in the online version at doi:10.1016/j.jhazmat.2025.138873.

Data availability

No data was used for the research described in the article.

References

[1] Song, S., Chen, K., Huang, T., Ma, J., Wang, J., Mao, X., Gao, H., Zhao, Y., Zhou, Z., 2023. New emission inventory reveals termination of global dioxin declining trend. J Hazard Mater 443, 130357.
[2] Liu, B., Han, Z., Liang, X., 2023. Dioxin emissions from municipal solid waste incineration in the context of waste classification policy. Atmos Pollut Res 14, 101842.
[3] Shunda Lin, X., Jiang, Y., Zhao, J., 2022. Yan, disposal technology and new progress for dioxins and heavy metals in Fly ash from municipal solid waste incineration: a critical review. Environ Pollut 311, 119878.
[4] Qu, W., Liu, X., Chen, J., Dong, Y., Tang, X., Chen, Y., 2020. Single-atom catalysts reveal the dinuclear characteristic of active sites in NO selective reduction with NH_3. Nat Commun 11, 1532.
[5] Li, G., Shen, K., Wang, L., Zhang, Y., Yang, H., Wu, P., Wang, B., Zhang, S., 2021. Synergistic degradation mechanism of chlorobenzene and NO over the multi-active center catalyst: the role of NO_2, Brønsted acidic site, oxygen vacancy. Appl Catal B Environ 286, 119865.
[6] Li, X., Niu, Y., Li, J., Yang, M., Chen, R., Shao, D., Zheng, X., Zhang, C., Qi, Y., 2023. Trace co doping improves NH_3-SCR performance and poisoning resistance of Ce-Mn-based catalysts. Chem Eng J 454, 140180.
[7] Kang, D., Shi, Q., Zhang, C., Zhao, P., Lyu, H., Huang, A., Shen, B., 2024. Modulation of acidic and redox properties of Mn-based catalysts by co doping: application to the synergistic removal of NO_x and chlorinated organics. Sep Purif Technol 339, 126695.
[8] Zhang, K., Luo, N., Huang, Z., Zhao, G., Chu, F., Yang, R., Tang, X., Wang, G., Gao, F., Huang, X., 2023. Recent advances in low-temperature NH_3-SCR of NO_x over Ce-based catalysts: performance optimizations, reaction mechanisms and anti-poisoning countermeasures. Chem Eng J 476, 146889.
[9] Sun, P., Wang, W., Weng, X., Dai, X., Wu, Z., 2018. Alkali potassium induced HCl/CO_2 selectivity enhancement and chlorination reaction inhibition for catalytic oxidation of chloroaromatics. Environ Sci Technol 52, 6438–6447.
[10] He, G., Gao, M., Peng, Y., Yu, Y., Shan, W., He, H., 2021. Superior oxidative dehydrogenation performance toward NH_3 determines the excellent low-temperature NH_3-SCR activity of Mn-based catalysts. Environ Sci Technol 55, 6995–7003.
[11] Wang, W.L., Meng, Q., Xue, Y., Weng, X., Sun, P., Wu, Z., 2018. Lanthanide perovskite catalysts for oxidation of chloroaromatics: secondary pollution and modifications. J Catal 366, 213–222.
[12] Wan, J., Tao, F., Shi, Y., Shi, Z., Liu, Y., Wu, G., Kan, J., Zhou, R., 2022. Designed preparation of nano rod shaped CeO_2-MnO catalysts with different Ce/Mn ratios and its highly efficient catalytic performance for chlorobenzene complete oxidation: new insights into structure–activity correlations. Chem Eng J 433, 133788.
[13] Zhu, X., Yuan, X., Song, Z., Peng, Y., Li, J., 2023. A dual-balance strategy via phosphate modification on MnO_2-CeO_2 for NO_x and chlorobenzene synergistic catalytic control. Appl Catal B Environ 342, 123364.
[14] Chen, J., Xu, W., Jiang, M., Chen, J., Jia, H., 2020. Polyoxometallate functionalizing CeO_2 via redox-etching precipitation to synergistically catalyze oxidation of gaseous chlorinated pollutants: from lab to practice. Appl Catal B Environ 278, 119263.
[15] Chen, J., Wang, C., Lv, X., Huang, G., Xu, W., Li, X., Jia, H., 2023. Pt/CeO_2 coated with polyoxometallate chainmail to regulate oxidation of chlorobenzene without hazardous by-products. J Hazard Mater 441, 129925.
[16] Wachi, K., Yabe, T., Suzuki, T., Yonesato, K., Suzuki, K., Yamaguchi, K., 2022. Selective oxidation of methane into formaldehyde and carbon monoxide catalyzed by supported thermally stable iron oxide subnanoclusters prepared from a diiron-introduced polyoxometalate precursor. Appl Catal B Environ 314, 121420.
[17] Misra, A., Zambrzycki, C., Kloker, G., Kotyrba, A., Anjass, M.H., Franco Castillo, I., Mitchell, S.G., Güttel, R., Streb, C., 2020. Water purification and microplastics removal using magnetic polyoxometalate-supported ionic liquid phases (magPOM-SILPs). Angew Chem Int Ed 59, 1601–1605.
[18] An, X., Tang, Q., Lan, H., Liu, H., Qu, J., 2019. Polyoxometalates/TiO_2 Fenton-like photocatalysts with rearranged oxygen vacancies for enhanced synergetic degradation. Appl Catal B Environ 244, 407–413.
[19] Gumerova, N.I., Rompel, A., 2018. Synthesis, structures and applications of electron-rich polyoxometalates. Nat Rev Chem 2, 0112.
[20] Liu, Y., Wang, F., Xie, F., Zheng, J., Lan, J., Guo, F., Sun, Y., Zhang, L., Liu, X., 2023. CaO-promoted lattice oxygen activation and antichlorine poisoning over mullite for catalytic chlorobenzene combustion. ACS Catal 13, 10340–10350.
[21] Zhao, L., Yang, Y., Liu, J., 2025. Insight into the reaction mechanism of NH_3-SCR and chlorobenzene oxidation over Mn-based spinel catalysts. J Hazard Mater 492, 138113.
[22] Li, Y., Hou, Y., Li, B., Yang, Y., Ma, S., Wang, B., Qin, G., Huang, Z., 2023. Inhibition mechanism of chlorobenzene on NH_3-SCR side reactions over MnO_x-CeO_2 confined titania nanotubes. Fuel 349, 128619.
[23] Mohammadi, A., Farzi, A., Thurner, C., Klötzer, B., Schwarz, S., Bernardi, J., Niaei, A., Penner, S., 2022. Tailoring the metal-perovskite interface for promotional steering of the catalytic NO reduction by CO in the presence of H_2O on Pd-lanthanum iron manganite composites. Appl Catal B Environ 307, 121160.
[24] Sun, P., Wang, W., Dai, X., Weng, X., Wu, Z., 2016. Mechanism study on catalytic oxidation of chlorobenzene over $Mn_xCe_{1-x}O_2$/H-ZSM5 catalysts under dry and humid conditions. Appl Catal B Environ 198, 389–397. https://doi.org/10.1016/j.apcatb.2016.05.076.
[25] Jiang, W., Yu, Y., Bi, F., Sun, P., Weng, X., Wu, Z., 2019. Synergistic elimination of NO_x and chloroaromatics on a commercial V_2O_5–WO_3/TiO_2 catalyst: byproduct analyses and the SO_2 effect. Environ Sci Technol 53, 12657–12667.
[26] Gan, L., Shi, W., Li, K., Chen, J., Peng, Y., Li, J., 2018. Synergistic promotion effect between NO_x and chlorobenzene removal on MnO_x–CeO_2 catalyst. ACS Appl Mater Interfaces 10, 30426–30432.
[27] Xia, G., Ye, Z., Xu, C., Wang, G., Zhang, Y., Yang, B., 2024. Synergistic catalysis of NO and chlorobenzene over Mn_3O_4-CeO_2 catalysts: acid sites, catalytic pathway and mechanism. J Environ Chem Eng 12, 113674.
[28] Silori, G.K., Chien, S.-C., Lin, L.-C., Ho, K.-C., 2024. A memory-rich conjugated microporous polymer-based electrochromic framework through two-in-one metal catalyst free route. Chem Eng J 484, 149417.
[29] Ye, Z., Wang, G., Giraudon, J., Nikiforov, A., Chen, J., Zhao, L., Zhang, X., Wang, J., 2022. Investigation of Cu-Mn catalytic ozonation of toluene: crystal phase, intermediates and mechanism. J Hazard Mater 424, 127321.
[30] Zhu, Y., Liang, W., Zhang, C., Bin, F., Tao, Q., 2024. Defect-rich regulatory activity strategy: disordered structure for enhanced catalytic interfacial reaction of chlorobenzene. Environ Sci Technol 58, 19385–19396.
[31] Ye, L., Lu, P., Xianhui, Y., Huang, H., 2023. Boosting simultaneous catalytic removal of NO_x and toluene via cooperation of lewis acid and oxygen vacancies. Appl Catal B Environ 331, 122696.
[32] Yang, H., Chen, A., Wang, F., Lan, T., Zhang, J., Hu, X., Shen, Y., Cheng, D., Zhang, D., 2024. Phosphotungstic acid as a dechlorination agent collaborates with CeO_2 for synergistic catalytic elimination of NO_x and chlorobenzene. Environ Sci Technol 58, 7672–7682.
[33] Li, Q., Huang, Z., Guan, P., Su, R., Cao, Q., Chao, Y., Shen, W., Guo, J., Xu, H., Che, R., 2017. Simultaneous ni doping at atom scale in ceria and assembling into well-defined lotuslike structure for enhanced catalytic performance. ACS Appl Mater Interfaces 9, 16243–16251.
[34] Zhang, Y.-C., Ullah, S., Zhang, R., Pan, L., Zhang, X., Zou, J.-J., 2020. Manipulating electronic delocalization of Mn_3O_4 by manganese defects for oxygen reduction reaction. Appl Catal B Environ 277, 119247.
[35] Deng, H., Kang, S., Ma, J., Wang, L., Zhang, C., He, H., 2019. Role of structural defects in MnO_x promoted by ag doping in the catalytic combustion of volatile organic compounds and ambient decomposition of O_3. Environ Sci Technol 53, 10871–10879.
[36] Gu, H., Lan, J., Liu, Y., Ling, C., Wei, K., Zhan, G., Guo, F., Jia, F., Ai, Z., Zhang, L., Liu, X., 2022. Water enables lattice oxygen activation of transition metal oxides for volatile organic compound oxidation. ACS Catal 12, 11272–11280.
[37] Zhang, X., Xu, Z., Jiang, M., Liu, Y., Han, Z., 2023. A confinement strategy for constructing $Ce_xMn_{1-x}O_2$ solid solutions with oxygen vacancies confined in interwoven titania nanotubes toward catalytic ozonation of 1,2-dichloroethane. J Environ Chem Eng 11, 109299.
[38] Liu, H., Li, X., Dai, Q., Zhao, H., Chai, G., Guo, Y., Guo, Y., Wang, L., Zhan, W., 2021. Catalytic oxidation of chlorinated volatile organic compounds over Mn-Ti composite oxides catalysts: elucidating the influence of surface acidity. Appl Catal B Environ 282, 119577.

[39] Xu, M., Liu, T., Gao, X., Jin, Q., Yang, J., Zhu, C., Wang, S., Xu, H., 2023. Simultaneous catalytic removal of NO and chlorobenzene over $MnCeSmSnO_X$: catalytic performance and removal mechanism. Chem Phys Impact 6, 100228.
[40] Liu, F., Li, J., Sohn, H.Y., Chen, C., Yang, J., Liu, X., Lan, Y., Zhang, W., Wang, Q., Liu, L., 2023. Redox on Mn-Ce interface and its effects on low temperature selective catalytic reduction for NO removal. Fuel 350, 128806.
[41] Wang, G., Ye, Z., Zhao, L., Liu, Y., Ji, J., Wang, J., 2022. Catalytic ozonation of toluene over amorphous Cu–Mn bimetallic oxide: influencing factors, degradation mechanism and pathways. Chemosphere 307, 135993.
[42] Zhang, C., Zhang, J., Shen, Y., He, J., Qu, W., Deng, J., Han, L., Chen, A., Zhang, D., 2022. Synergistic catalytic elimination of NO_x and chlorinated organics: cooperation of acid sites. Environ Sci Technol 56, 3719–3728.
[43] Liu, J., Li, X., Li, R., Zhao, Q., Ke, J., Xiao, H., Wang, L., Liu, S., Tadé, M., Wang, S., 2017. Facile synthesis of tube-shaped Mn-Ni-Ti solid solution and preferable Langmuir-Hinshelwood mechanism for selective catalytic reduction of NO_x by NH_3. Appl Catal Gen 549, 289–301.